Study on the life cycle of ice crystal cloud over the Taklimakan desert using multi-source data

Lian Su[1,2], Chunsong Lu[3], Jinlong Yuan[3], Kenan Wu[4], Tianwen Wei[3], Xiaofei Wang[5], Qing He[5,6], Mohamed Elshora[4], Xi Luo[1,2], Xinyang Li[1,2] and Haiyun Xia[3,4]

[1]National Laboratory on Adaptive Optics, Chengdu 610209, China
[2]Institute of Optics and Electronics, Chinese Academy of Sciences, Chengdu 610209, China
[3]School of Atmospheric Physics, Nanjing University of Information Science and Technology, Nanjing 210044, China
[4]School of Earth and Space Science, University of Science and Technology of China, Hefei 230026, China
[5]Xinjiang Uygur Autonomous Region Meteorological Service, Urumqi 830002, China
[6]Institute of Desert Meteorology, China Meteorological Administration, Urumqi 830002, China

Correspondence to: Haiyun Xia (hsia@ustc.edu.cn)

Abstract. Using a coherent Doppler wind lidar, the whole process of formation and decomposition of ice crystal cloud was recorded in Minfeng (37.06 °N, 82.69 °E) on the southern edge of the Taklimakan Desert (TD) from 5 to 6 February 2022. Combined with ERA5 and MERRA-2 reanalysis data, FY-4A and Himawari-8 meteorological satellite data, local meteorological data, and HYSPLIT model, the evolution process of ice crystal clouds affected by the wind profile, dust aerosol, turbulence, temperature, humidity, and terrain was analyzed. The results show that the uniquely relatively enclosed basin topography of the TD, coupled with the feeble turbulence and robust downdrafts at night, constrains the upward supply of water vapor and dust aerosols. As a result, the base height of the ice crystal clouds is maintained at approximately 3 km. Dust aerosols can act as effective ice nuclei, which catalyze the formation of ice crystal clouds and inhibit the occurrence of liquid precipitation. The continuous evolution of ice crystal clouds was well studied with multiple meteorological data, which improves the understanding of dust-cloud-atmosphere interactions in the desert hydrological cycle.

1 Introduction

Atmospheric ice nuclei (IN) refer to aerosol particles suspended in the atmosphere, which can condense water vapor or freeze supercooled droplets to form ice crystals (Vali, 1985). IN can have a huge impact on physical processes such as radiative transfer, precipitation, and cloud electrification (Heymsfield, 2005), thus they have significance in studying the precipitation process of natural cold clouds (Morris et al., 2004), artificial weather modification (Demott et al., 1983), the interaction between clouds and aerosols, and even global climate change (Ramanathan et al., 2001; Zeng et al., 2009).

The huge global emission of mineral aerosol dust is one of the important sources of IN (Kanji et al., 2017), which plays an important role in the dust-aerosol-cloud-precipitation interaction (DACPI). There is a significant correlation between IN and mineral aerosol dust (Klein et al., 2010). Under certain conditions, dust can not only inhibit rainfall but also enhance rainfall (Huang et al., 2014). Rosenfeld et al. (2001) found that when the Sahara desert dust acts as effective cloud condensation nuclei

(CCN) or IN, the increase of dust concentration leads to the decrease of cloud droplet size, which can reduce the efficiency of cloud droplet coalescence and inhibit the occurrence of precipitation. At the same time, the reduction in precipitation will lead to further drying of the soil, which may increase the dust content in the desert and provide a possible feedback loop to further

35 reduce precipitation (Rosenfeld et al., 2001). When desert dust acts as an effective IN, it can make the top of the convective cloud have the ability to freeze, so as to promote the occurrence of ice precipitation, rather than inhibit the occurrence of warm rain (Rosenfeld et al., 2011).

It is difficult to grasp the regional and local changes of ice crystal clouds by using only one kind of data, whereas the combination of multi-source data can fully discover the trend of cloud change. Coherent Doppler wind lidar (CDWL) has the

40 characteristics of high temporal and radial spatial resolution (Zhang et al., 2021), small detection blind area, high detection accuracy and real-time acquisition of three-dimensional motion information of the atmosphere. Based on these characteristics, the CDWL can obtain the wind field information (Liu et al., 2020) in the cloud and distinguish the vertical distribution of clouds and aerosols, which makes it possible to capture the evolution process of clouds. Therefore, CDWL has been utilized to study DACPI caused by dust transported from the desert (Chouza et al., 2016; Westbrook et al., 2010; Westbrook and

45 Illingworth, 2013; Ansmann et al., 2009; Seifert et al., 2010). The large-scale observation of meteorological satellites can obtain various cloud products from satellite-based data, and other valuable meteorological products can be obtained through atmospheric reanalysis techniques. The combination of these large amounts of product data makes it possible to analyze the large-scale changes of clouds, so as to capture the overall regional change process of clouds (Yoshida et al., 2010; Alexander and Protat, 2018). At present, there are many studies on the changes of local clouds and weather caused by the transport of

50 dust aerosols in the study sites far away from the desert (Seifert et al., 2010; Ansmann et al., 2005). However, due to the factors such as equipment performance, harsh environmental climate, and desert human resource allocation, it is not sufficient to study the influence of dust aerosols on local cloud and weather changes in the desert where dust transport originates.

In order to study the desert meteorology, such as wind conditions and DACPI, a long-term and stable continuous observation experiment was carried out in Minfeng County by using the CDWL, and a complete process of ice crystal cloud evolution was

55 observed from February 5 to 6, 2022. The effects of wind, dust aerosol, turbulence, temperature, humidity, terrain and other factors on the evolution of ice crystal clouds were analyzed by multi-source data. This paper is organized as follows: the study site and datasets are described in Sect. 2. The observations of various data are presented and analyzed in Sect. 3. Finally, a conclusion is drawn in Sect. 4.

2 Site and data resources

60 ### 2.1 Study site

The Taklimakan Desert (TD), located in the Tarim Basin, is the world's second largest shifting sand desert and the largest desert in China. The terrain corresponds to high elevation in the north, with an average elevation of more than 1 km, as shown in Figure 1. The TD is surrounded by three mountains, and the near-surface wind regimes is characterized by the prevailing

northeast wind (Sun and Liu, 2006), the special terrain makes it very easy to form dust storms. The observation experiment
65 was carried out in Minfeng County (37.06 °N, 82.69 °E), which is located in the southern edge of the TD and the northern foot
of the Kunlun Mountains. The climate of Minfeng belongs to a typical temperate arid climate with sufficient sunshine and
scarce precipitation. When the cold air of different intensity invades, due to the blocking effect of the Tibet Plateau, the study
site Minfeng is located in the convergence and ascending range of the east and west airflow (Liu et al., 2019). As a result, the
wind-sand activity in this area is extremely strong, making it one of the regions with a high frequency of sandstorm weather
70 in China (Yang et al., 2016). A digital elevation map of the study site is also added in Figure S1.
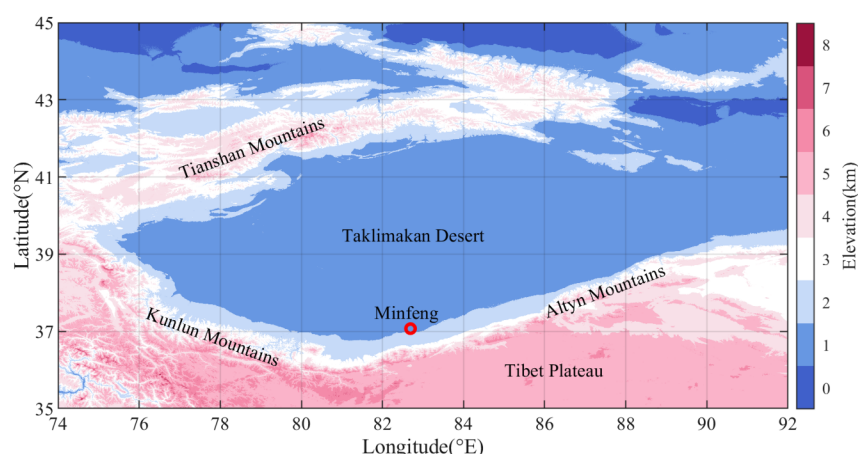
Figure 1: The elevation map of Taklimakan Desert. The red circle represents the study site, Minfeng.

2.2 CDWL measurements

A CDWL conducted long-term stable detection experiments on the Taklamakan Desert, the process formation of ice crystal
75 cloud was observed from 5 to 6 February, 2022. It is operated at an eye-safe wavelength of 1.5 μm. The pulse energy of the
laser is 130 μJ. The radial spatial resolution of the CDWL is 30 m. The sampling rate of the analog-to-digital converter (ADC)
is 500 MS s^{-1}. The key parameters are listed in Table 1. During the experiment, the lidar operates in a velocity azimuth display
(VAD) scanning mode with a period of 1 minute. The elevation angle is fixed at 70°. The azimuth angle changes from 0° to
300° with a step of 12°. The carrier-to-noise ratio (CNR) directly reflects the data quality of CDWL (Yuan et al., 2020). To
80 ensure the reliability of the data, the CDWL data with a CNR less than -17 dB were filtered out. Banakh et al. (2017)
described the calculation method and error analysis of turbulent kinetic energy dissipation rate (TKEDR) (Banakh et al.,
2017). Li et al. (2023) introduced the inversion of backscattering coefficient (BSC) in detail (Li et al., 2023). Wei et al. (2019)
analyzed the error of wind speed and wind direction (Wei et al., 2019). The planetary boundary layer height (PBLH) is
calculated by using the TKEDR method (Wang et al., 2021). Su et al. (2024) provided a detailed explanation of the parameter
85 inversion method in the article (Su et al., 2024a).

In a cloud system with a scale of hundreds kilometers, the evolution process of each part of the cloud system is synchronized as a whole. As the development of the cloud system is accompanied by the advection, when the cloud system passes over the CDWL site, the CDWL can sample different parts of the cloud system at different times, which means that the obtained data is corresponding to the different development stages of the cloud system. Therefore, the CDWL detection method as a fixed-space Euler method can be used to study the evolution of cloud systems. In the previous studies, this type of lidar has been used in the research of atmospheric turbulence (Jiang et al., 2022), bioaerosol (Tang et al., 2022), planetary boundary layer height (Wang et al., 2022; Su et al., 2024a; Su et al., 2024b), simultaneous detection of wind and rain (Wei et al., 2019), thundercloud structure (Wu et al., 2023), wind shear (Yuan et al., 2022a; Yuan et al., 2020) and so on.

Table 1: Key parameters of CDWL

Parameter	Value
Wavelength	1.5 μm
Pulse energy	130 μJ
Pulse repetition rate	10 kHz
Diameter of telescope	100 mm
Radial spatial resolution	30 m
Azimuth scanning range	0 ~ 360 °
Zenith angle	70 °
Sample rate of ADC	500 MS/s

2.3 Other data

ERA5 is the fifth-generation global climate reanalysis dataset from the European Centre for Medium-Range Weather Forecasts (Hersbach et al., 2020). In this paper, u-v wind vector, specific cloud ice water content (CIWC), temperature and relative humidity in ERA5 are used to study the cloud movement trend over the entire TD region. The dataset used has a spatial resolution of 0.25° × 0.25° and a temporal resolution of 1 hour.

MERRA-2 (Modern-Era Retrospective Analysis for Research and Applications, Version 2)is the atmospheric reanalysis of the modern satellite era produced by NASA's Global Modeling and Assimilation Office (Gelaro et al., 2017). The aerosol assimilation reanalysis datasets in MERRA-2, including dust dry and wet deposition, dust sedimentation, dust emission, and dust convection scavenging, were used to analyze the spatio-temporal variations of dust aerosols over the TD. The spatial resolution and temporal resolution of the data set used were 0.5° × 0.625° and 1 hour, respectively.

Fengyun-4A (FY-4A) is a new generation geostationary meteorological satellite in China (Yang et al., 2017), equipped with an advanced geostationary radiation imager (AGRI) that can offer a variety of cloud products in the study area. In this paper, the cloud top temperature product (CTT) and cloud phase product (CLP) with a horizontal spatial resolution of 4 km and temporal resolution of 15 minutes are used to analyze the change of cloud top temperature and cloud phase, respectively. The

470 nm, 650 nm and 830 nm three-band data in the FY-4A L1 dataset with a horizontal spatial resolution of 1 km are used to

110 synthesize pseudo-color images. The cloud phase product of FY-4A is reasonably consistent with MODIS and Himawari-8 (Lai et al., 2019).

Himawari-8 satellite (Bessho et al., 2016), launched by the Japan Meteorological Agency, is equipped with an Advanced Himawari Imager (AHI) that employs a sophisticated cloud classification algorithm to discern various cloud types. The spatial and temporal resolutions of the Himawari-8 satellite data are 5 km and 10 minutes, respectively.

115 To identify aerosol sources and spatial transport paths, the HYbrid Single-Particle Lagrangian Integrated Trajectory (HYSPLIT) (Stein et al., 2015) model was used. The HYSPLIT model was configured to perform 24 hour back trajectory calculations at an altitude of 3 km above the study site, utilizing meteorological data from the Global Data Assimilation System (GDAS) with a spatial resolution of 1°.

The meteorological data provided by the Minfeng County Meteorological Bureau is used to analyze near-surface

120 meteorological changes, including temperature, relative humidity, horizontal visibility, horizontal wind speed, and horizontal wind direction.

3 Observations and analysis

In order to analyze the formation process of ice crystal clouds more directly, and combined with the dust transport process caused by atmospheric turbulence movement, this paper divides the life cycle of ice crystal clouds into four-time stages (Field,

125 1999; Sullivan et al., 2022): pre-formation, forming, formed, decomposition. The time stages are divided as shown in Table 2.

Table 2: Evolution process of ice crystal cloud

Stage	Time range
Stage-1 Pre-formation	5 February 00:00 LT to 12:00 LT
Stage-2 Forming	5 February 12:00 LT to 22:00 LT
Stage-3 Formed	5 February 22:00 LT to 6 February 10:00 LT
Stage-4 Decomposition	6 February 10:00 LT to 24:00 LT

3.1 Phenomena observed by the FY-4A satellite and Himawari-8 satellite

In this section, firstly, a cloud transit was observed by using the synthetic image of FY-4A. Subsequently, the temperature and

130 phase changes of the cloud were analyzed by using FY-4A's CTT and CLP data. Finally, himawari-8 cloud classification data were employed to cross-verify FY-4A's observational results.

3.1.1 Cloud distribution

As shown in Fig. 2, the pseudo-color images synthesized by three bands in the FY-4A L1 dataset show the partial distribution of clouds over the TD on February 6, 2022. Taking into account the sunrise and sunset time of the day, the starting time of the displayed image is at 11:30 LT. As can be seen from Fig. 2a, a cloud system with a scale of hundreds of kilometers is distributed near the study site, and part of the surface state can be seen through the cloud system. Before 13:30 LT, the study site was covered by clouds. After 14:30 LT, the clouds in the study site dissipated gradually.
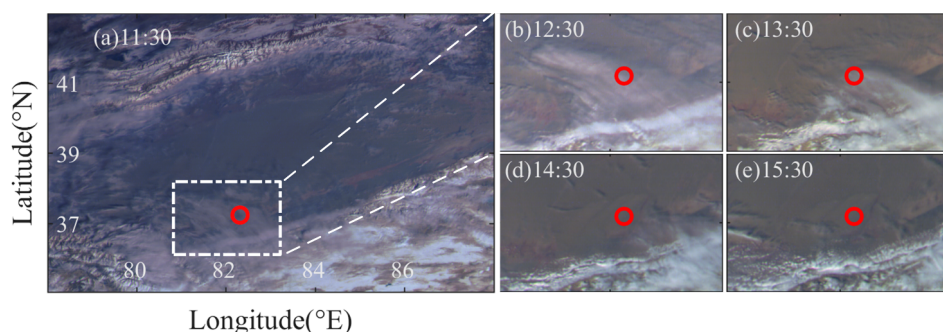
Figure 2: Cloud distribution of FY-4A over the Taklimakan Desert from 11:30 to 18:00 LT (UTC+8) on 6 February 2022. The red circle symbol represents the study site Minfeng. The white box represents the drawing area of the subgraph.

3.1.2 Cloud top temperature and cloud phase

The formation of ice crystal clouds can affect the temperature of cloud tops (Li et al., 2017). Fig. 3 shows the probability distribution of cloud phase and cloud top temperature at the study site over the whole observation time. It can be seen from the figure that the ice crystal cloud is formed under relatively warm temperature conditions (-10 °C to -17.5 °C), and dust aerosols can form IN under such temperature conditions (Crawford et al., 2012; Murray et al., 2012). When the temperature is lower than -27.5 °C, the cloud phase changes from a mixed phase to an ice phase gradually. When the temperature is lower than -37.5 °C, the cloud only has an ice phase.
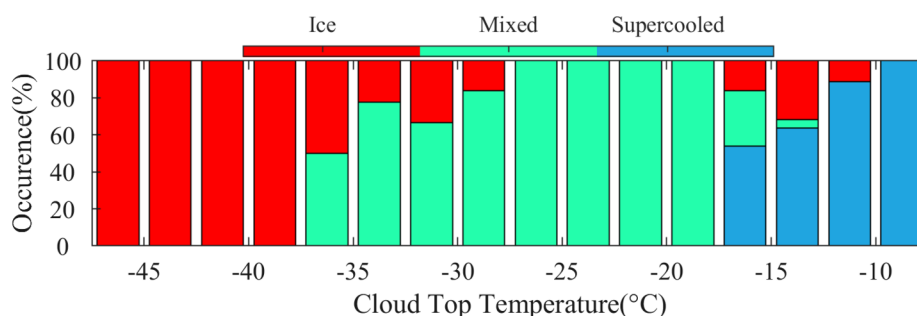
Figure 3: The occurrence probability of cloud phase types at different cloud top temperatures of FY-4A in the study site of Minfeng from 5 to 6 February 2022 (UTC+8).

Fig. 4 shows the change process of cloud phase in the study site from 5 to 6 February, 2022. During Stage-1, it can be seen that a cloud system passed by the study site and completely dissipated. During Stage-2, the study site was in a cloud-free state

before 20:00 LT, However, from 20:00 to 22:00 LT, the study site began to be covered by clouds and under relatively warm temperature conditions (in Fig. 3), the cloud phase transitioned from supercooled water phase to ice phase. Therefore, this

155   phenomenon indicates that dust aerosols can act as IN and participate in the formation of ice crystal clouds, as observed in previous studies (Murray et al., 2012; Moore and Molinero, 2011). During Stage-3, the study site was nearly continuously covered in clouds. The phase state of the cloud is dominated by mixed phase and ice phase, which indicates that this cloud system is composed of ice crystal clouds and constitutes a complete advection cloud system. It is worth noting that the AGRI may identify some ice clouds as mixed-phase clouds (Lai et al., 2019), while current Himawari-8 observations predominantly

160   show cirrus cloud (in Fig. 6), which coincidentally cross-validates the FY-4A's observational results. During Stage-4, the mixed phase cloud completely dissipated after 14:30 LT with the cloud advection movement.
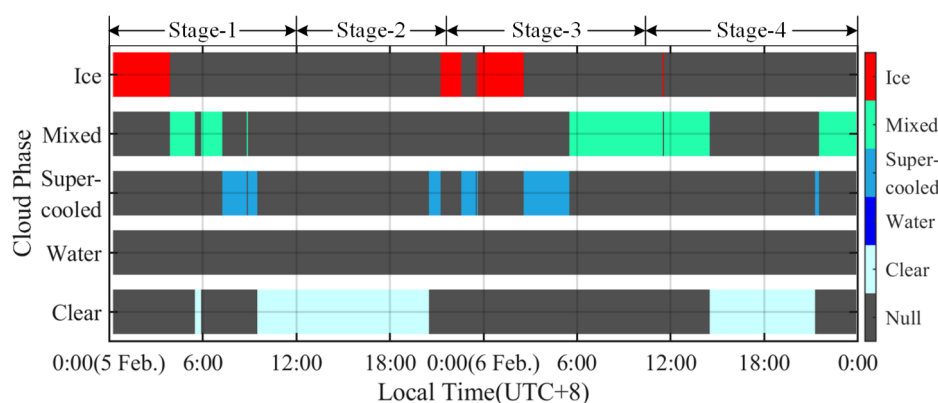
Figure 4: Cloud phase distribution of FY-4A at the study site Minfeng from 5 to 6 February 2022 (UTC+8). The value of Null and Clear represent the background color and cloudless, respectively. The cloud phase types include ice (red), mixed (aquamarine),
165   **supercooled water (sky blue) and water (blue).**
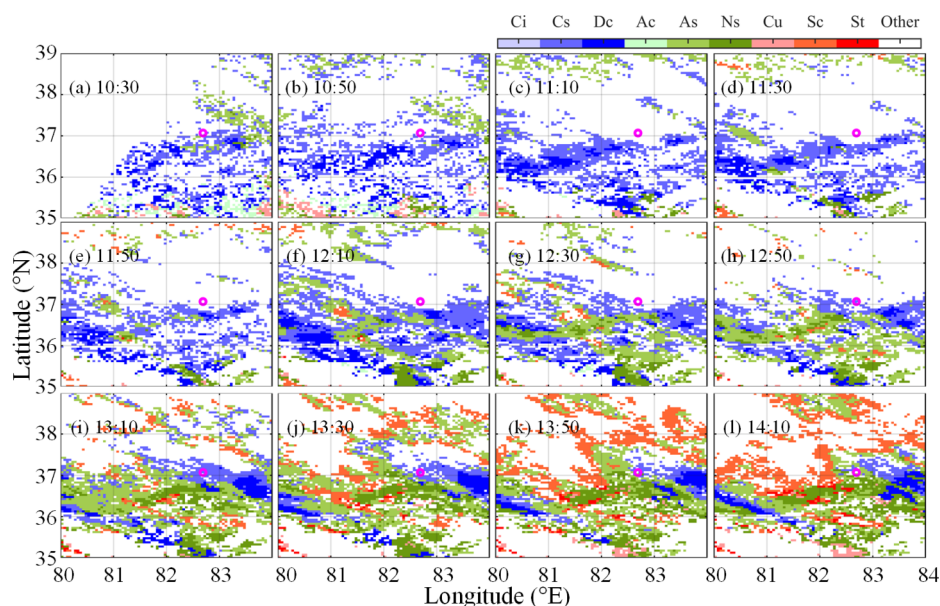
Figure 5: The Himawari-8 satellite observed changes in cloud type at the study site every 20 minutes from 10:30 to 14:10 LT (UTC+8) on 6 February 2022. The purple circle symbol represents the study site Minfeng. Cloud types are distinguished by different colors. The cloud type of Ci, Cs, Dc, Ac, As, Ns, Cu, Sc, St represent cirrus, cirrostratus, deep convection, altocumulus, altostratus, nimbostratus, cumulus, stratocumulus, stratus, respectively.

3.2 Lidar results and comprehensive analysis

In this section, multi-source data are used to comprehensively analyze the life cycle and influencing factors of the ice crystal clouds. Fig. 6 shows the continuous observation results of CDWL, ERA5 and FY-4A from 5 to 6 February, 2022. The u-v wind vector in ERA5 was used to analyze the boosting effect of the special terrain factors (Lloyd et al., 2015; Rogers and Vali, 1987) on the formation of ice crystal clouds. Fig. 6 shows the 24 h HYSPLIT backward trajectory results of dust transport. Each stage of the ice crystal cloud life cycle is analyzed as follows.

Stage-1: Pre-formation. The wind created horizontal transport conditions for dust aerosols. Near the surface (below 1 km), firstly, a lower stable nocturnal boundary layer is formed due to the weak turbulent motion (Fig. 6f), which limits the transmission of near-surface dust aerosols to the upper atmosphere. Secondly, in Fig. 6d, the horizontal wind speed near-surface is high from 0:00 to 5:00 LT, but then the wind speed decreases to a calm state, which can lead to the suspension of dust aerosols (as shown in Fig. 6a and Fig .6b of dust layer). Then, in terms of wind direction, the westerly wind prevails in the upper atmosphere from 5:00 to 12:00 LT, and the easterly wind prevails near the ground. The opposite wind direction can further separate the high-altitude water vapor from the near-surface dust aerosol. Additionally, the CNR or backscattering coefficient can be used as an indicator of aerosol concentration (Pea et al., 2013; Heese et al., 2010), and the BSC in regions of the TD with relatively strong dust intensity is distributed from $2 \cdot 10^{-6}$ to 10^{-5} $m^{-1} \cdot sr^{-1}$ (Shuoqiu and Xiaoyan, 2020). Therefore, from 6:00 to 12:00 LT, as depicted in the Fig. 6a, the CNR value in box A (below 1.5 km) is greater than the above value, correspondingly, the BSC value (from $2 \cdot 10^{-6}$ to $4 \cdot 10^{-6}$ $m^{-1} \cdot sr^{-1}$) of Fig. 6b within this temporal and spatial interval falls within the BSC range for dust aerosols, which proves that there is a dust layer here. Specifically, as depicted in Fig. S3a, a horizontal convergence airflow was formed in the TD. On February 5 at 10:00 LT, the local visibility reached the minimum value of 6 km and the situation at that time belonged to the dust weather, as indicated in Fig. S2.

Stage-2: Forming. The turbulence and wind can provide an opportunity for dust aerosols to contact supercooled water, thereby promoting the formation of ice crystal clouds. The PBLH can reflect the atmospheric environmental capacity of the region and the degree of vertical diffusion of pollutants (Holtslag and Boville, 1993), and plays an important role in the transport and diffusion of IN. After sunrise, with the increase of solar radiation (Fig. 6i), the turbulent activity gradually becomes active and a convective mixed boundary layer with a maximum height of 3 km is formed (Fig. 6f). At the same time, the near-surface horizontal wind speed increases gradually, and the horizontal wind direction at low altitude turns from southwest to north (Fig. 6e and Fig. S3e). Firstly, it can be found in Fig. S3g and Fig. S1 that the change of wind direction can create the conditions for the transport of dust aerosols along the Kunlun Mountains to the upper atmosphere. Secondly, the values of PBLH, BSC and CNR have an uplift process, the 24-hour HYSPLIT backward trajectory results shown in Fig. 7 clearly show the climbing

200   process of dust aerosols. The dust emission in Fig. S4k-l is also greater than 0.5 ug m⁻² s⁻¹, and there is basically no dry and wet deposition of dust here (Fig. S4a-e). Additionally, the relative humidity in Fig. 6h decreased rapidly near the height of 3 km. Then, in Fig. 6i and Fig. 6g, the temperature slowly rises to -15 °C and the weight of ice in the cloud increases significantly at 600 hPa (form 0.12 to 4.29 mg/kg). Meanwhile, in Fig. 6c, the cloud top height rose from around 2.37 km to over 3 km after 20:30 LT. Finally, combined with the CLP and CTT data of FY-4A in Fig. 4, it can be seen that dust aerosols can act as

205   effective IN and participate in the formation of ice crystal clouds.

Stage-3: Formed. In this stage, the ice crystal cloud has been stably formed and transported to a wide horizontal range, and most cloud types are cirrus (Fig. 5). When the lidar beam hits the ice crystal cloud, the distribution of the crystal base surface makes the laser energy decay rapidly, thus forming a very strong backscattering signal (He et al., 2021; Westbrook et al., 2010). Clouds can be detected from the BSC values by selecting a threshold of 10^{-5} m⁻¹ sr⁻¹ (Manninen et al., 2018; Harvey et

210   al., 2013). In the experiment, judging from the thin layers of the CNR (> −5 dB), BSC (≥ 10^{-4} m⁻¹ sr⁻¹) and CIWC (≥ 0.12 mg/kg) at about 3 km, the laser beam does not penetrate the ice crystal cloud, which is the parent cloud of the ice virga (Wu and Yi, 2017; Cheng and Yi, 2020). In terms of turbulence in Fig. 6f, during the night and morning, there is a stable nocturnal boundary layer with low temperature and weak turbulence. The updraft air at low altitude (Fig. 6c) against downdraft air at high altitude balances the gravity of the ice crystal cloud, supporting the continuous growth of the ice crystal cloud. In terms

215   of relative humidity, water vapor competition can be more intense due to the generation of a large number of ice crystals, making it more difficult to increase the size of ice crystals, thus maintaining the existence of ice crystal clouds (Li et al., 2011; Tao et al., 2012). Therefore, it can be found from Fig. 6h that the relative humidity of the atmosphere above 3 km is always maintained below 40% during this stage. In addition, since the underlying surface of the atmosphere is a dry desert and the terrain is a relatively enclosed basin terrain surrounded by mountains on three sides, the turbulent activity at night is weak, and

220   a significant downdraft is sustained throughout the stage. This situation results in the attenuation of the upward transport of water vapor and dust aerosols. As a result, the cloud base height of the ice crystal cloud consistently stays at a relatively low height of around 3 km (Wu and Yi, 2017; He et al., 2023; Seifert et al., 2010). It is worth noting that in Fig. 6c, the gradual thickening of the cloud layer can increase the probability of collision and coalescence of ice crystals, thus creating conditions for ice phase precipitation in the Stage-4.

225
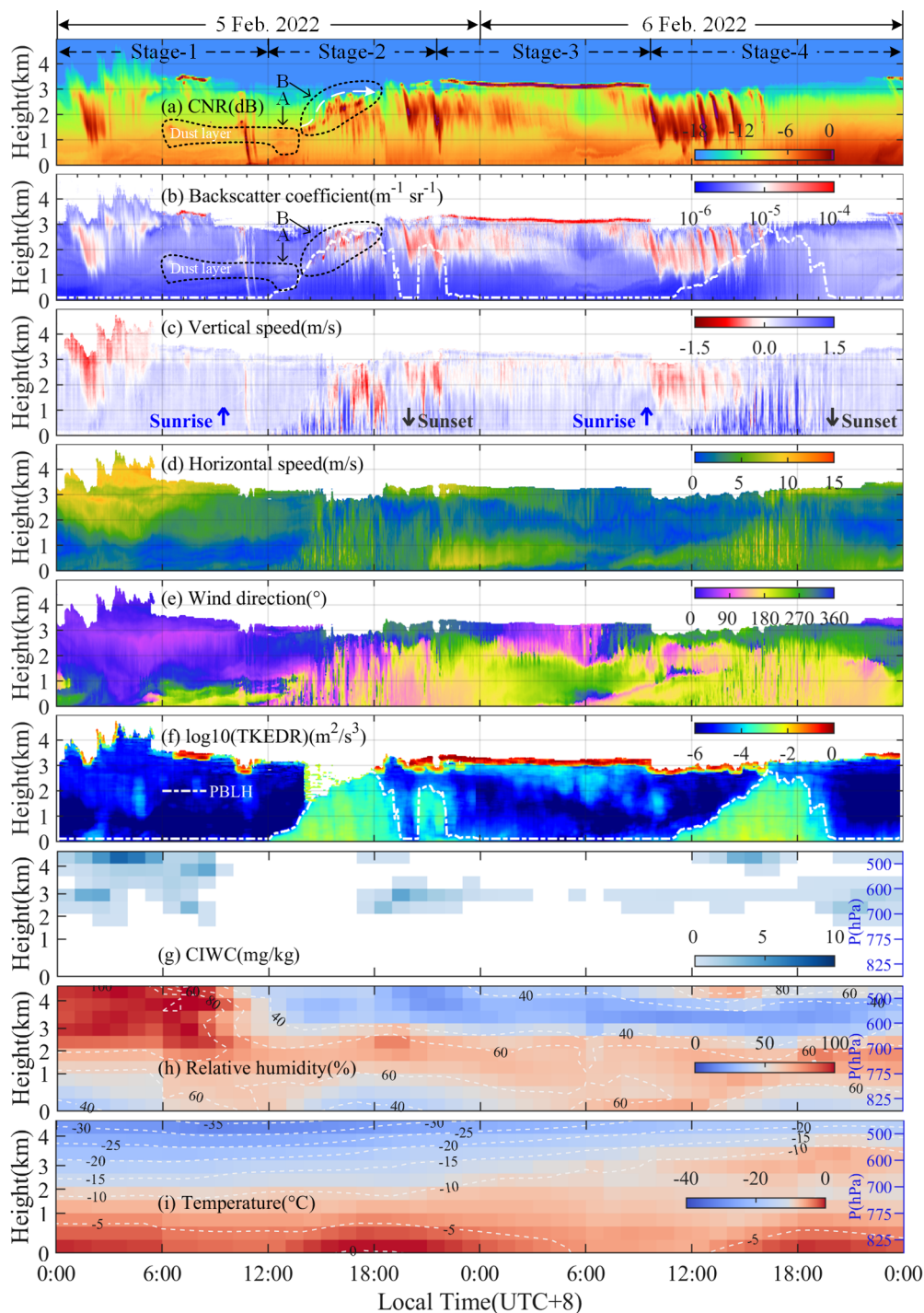
Figure 6: The ice crystal cloud episode was detected based on muti-source data, shch as CDWL, ERA5 and FY-4A, from 5 to 6 February 2022 (UTC+8). (a) CNR, (b) backscatter coefficient, (c) vertical wind speed, (d) horizontal wind speed, (e) horizontal wind direction, (f) log10(TKEDR), (g) specific cloud ice water content, (h) relative humidity, (i) temperature. The height represents the height above the ground of the lidar site. The four stages of the ice cloud life cycle are labelled in Fig. 6a. In Figs.5a and 5b, the

20

230   **dotted boxes A and B represent the existing dust layer and the upward transport process of dust aerosol, respectively. The positive
       vertical wind speed in Fig. 6c represents the rising speed, and vice versa; Cloud top heights below 5 km are marked with black lines
       in Fig. 6c. The time of sunrise and sunset is also marked with arrow symbols in Fig. 6c. In Fig. 6e, 0° represents the wind blows to
       the north. The PBLH is denoted by white dashed lines in Fig. 6b and Fig. 6f, respectively. The temperature and relative humidity
       contours in Fig. 6h and Fig. 6i are denoted by light gray dashed lines.**

235   Stage-4: Decomposition. With the rise of the sun, the temperature gradually increases to form a mixed boundary layer

       dominated by downward airflow, and the ice crystal cloud begins to transform into a mixed phase cloud and sink downward.

       The ice virga layer refers to the ice crystal precipitation layer formed by vaporization or liquefaction before falling to the

       ground (Westbrook and Illingworth, 2013; Gultepe et al., 2017). By analyzing the CNR and BSC values from 10:00 to 16:00

       LT, it is obvious that the large-grained ice crystals growing by coalescence rush down from 3 km to 1 km under the function

240   of gravity conditions, forming an ice virga. When the ice virga sinks down to about 1 km, as shown in Fig. 6a, due to the

       relatively dry (Fig. 6h-i) and strong northeast wind blowing from the desert hinterland and the frictional effects of air resistance,

       the ice virga evaporates before reaching the ground. At the same time, the amounts of dust from wet and dry deposition are

       very limited (Fig. S5a-d), however, dust sedimentation is evident (Fig. S5f-i). The maximum falling velocity of ice virga during

       the observation period is 1.38 m/s, which agrees well with previous observations (Ansmann et al., 2008; Abshire et al., 1974).

245   Note that the evaporation of ice crystals pushes the dust aerosol down to the lower layer, making the CNR increase below 1

       km, reducing the relative humidity to below 60% at 825 hPa, and causing the presence of dust convection scavenging near the

       study site (Fig. S5s-t).

       Compared with Figure 4, the distribution of ice crystal clouds observed by CDWL is generally consistent with that of FY-4A.

       Due to the fact that the FY-4A observation focuses on the cloud top state and it's horizontal spatial resolution and time

250   resolution are much coarser than the CDWL. Additionally, by using the nine pixels closest to the study site in both FY-4A and

       ERA5 datasets as the subject of the study, so the cloud results are also slightly different. As a comparison, the observation

       results of Himawari-8 satellite and local meteorological instruments are shown in Figure 5 and Figure S2. From the observation

       results of these data, it can be seen that there is the same change trend with the CDWL data.

       Fig. 8 shows two typical power spectrum of the vertical speed during the ice phase precipitation events observed by CDWL.

255   Fig. 8a-g shows a precipitation event that occurred on 5 February, a light precipitation hits the ground when the wind below 1

       km is weak. In another different case as shown in Fig. 8h-n, the precipitation failed to touch the ground due to the higher

       temperature and stronger wind below 1 km. As shown in Fig. 8, the difference between the speed of the aerosol and that of the

       ice crystal is not obvious. This may suggest that, no liquid precipitation occurs, since the Doppler double-peak power spectrum

       structure caused by the difference between wind speed and rain speed is not observed (Wei et al., 2019).
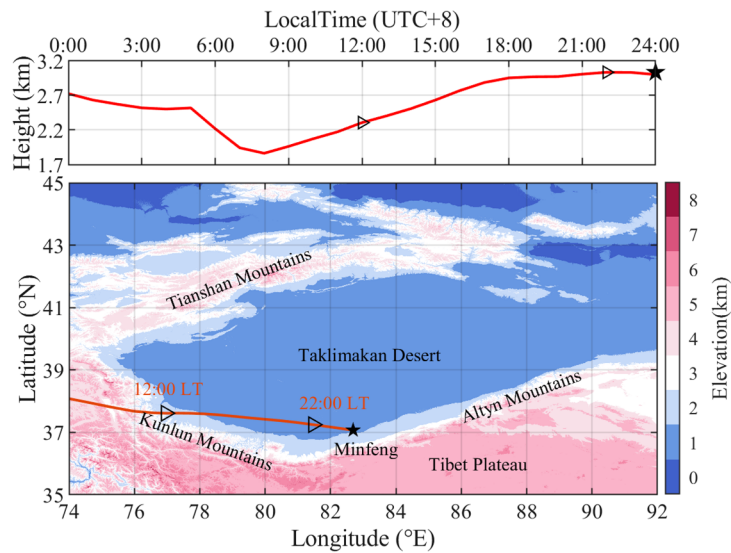
260

Figure 7: The 24 h HYSPLIT backward trajectory results of dust transport calculated at 24:00 LT (UTC+8) on 5 February 2022. The starting location is set at 3 km above the study site Minfeng. The study site exhibits a distinct upward dust transport process between 12:00 and 22:00 LT. (a) dust aerosol vertical transport path, (b) dust aerosol horizontal transport path.
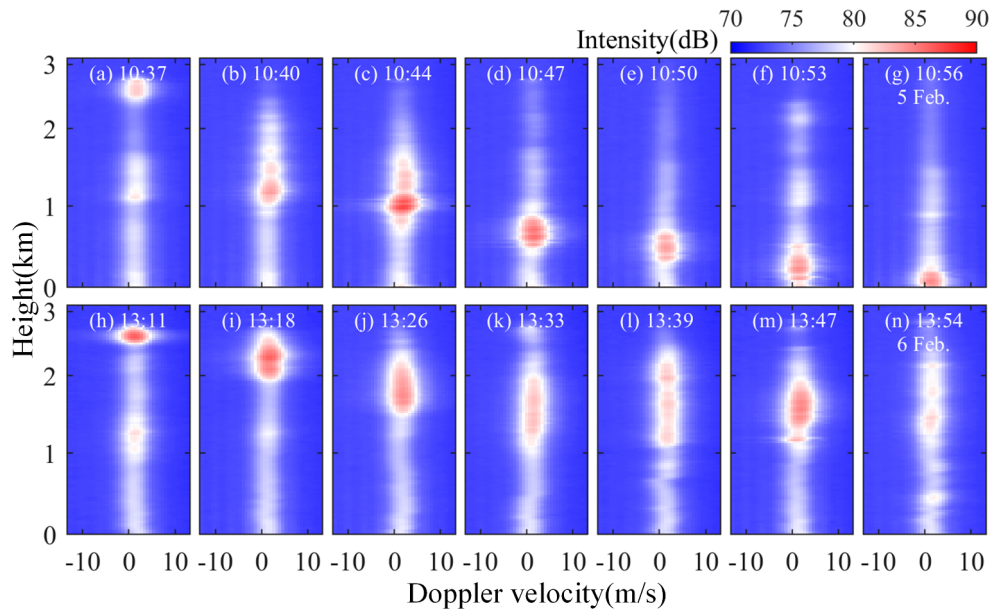
265 **Figure 8: The power spectrum observation results of two typical ice phase precipitation events were obtained during the lidar experiment. (a-g) from 10:37 to 10:56 LT (UTC+8) on 5 February 2022, (h-m) from 13:11 to 13:57 LT on 6 February 2022.**

5 Conclusions

In this study, multi-source data were used to analyze a complete ice crystal cloud evolution process on the southern edge of Taklimakan Desert from 5 to 6 February 2022. The results indicated that the aerosol-cloud-precipitation interaction plays a

270   important role in the life cycle of ice crystal clouds. As an effective IN, dust aerosols make more water vapor distributed into dust particles, and the limited water content in the desert atmosphere will lead to fierce competition for water vapor, thus increasing the difficulty of the growth of ice crystal particle size and inhibiting the occurrence of precipitation. The terrain of Taklimakan Desert is a relatively enclosed basin terrain surrounded by mountains on three sides, and the complete formation of the ice crystal cloud is at night when the turbulent activity of the stable nocturnal boundary layer is weak and the underlying

275   surface of the atmosphere is a dry desert, which greatly weakens the upward transport of water vapor and dust aerosol, thus making the cloud base height maintained at around 3 km. Due to the enhancement of solar radiation, the heterogeneous nucleation makes the cloud top temperature rise slowly, and due to the lack of water vapor and dust aerosol supplement, the ice crystal cloud begins to decompose and produce ice precipitation, which evaporates before reaching the ground.

Overall, the results not only reveal the transmission and diffusion mechanism of dust in the Taklimakan Desert, but also reflect

280   the important role of terrain, turbulence and wind in the life cycle of ice crystal clouds in a more comprehensive and detailed way, thus improving the understanding of the dust-cloud-atmosphere interaction in the desert hydrological cycle. Since CDWL cannot obtain cloud phase information directly, in the future research, we plan to combine polarization lidar and weather radar to classify clouds and aerosols (Ma et al., 2015; Yin et al., 2021; Wu et al., 2015; Yuan et al., 2022b), and to further understand the formation mechanism of ice crystal cloud in the desert.

285   *Data availability.* Data supporting the results are available in the supporting information. The ERA5 data sets are publicly available from the ECMWF website at https://doi.org/10.24381/cds.bd0915c6. The MERRA-2 data used can be downloaded from https://doi.org/10.5067/HM00OHQBHKTP. The FY-4A satellite data are available on the National Satellite Meteorological Center (NSMC) website at https://satellite.nsmc.org.cn. The Himawari-8 data can be downloaded from https://www.eorc.jaxa.jp/ptree/index.html. The aerosol source and transport path can be visualized on the website:

290   https://www.ready.noaa.gov/HYSPLIT.php. All the above data need to be registered before downloading. The CDWL datas (Su et al., 2024c) can be downloaded from https://doi.org/10.6084/m9.figshare.25432984.

Author contributions. H.X., L.S., and J.Y. planned the campaign; L.S., X.W., and Q.H. performed the measurements; L.S., C.L., J.Y., K.W., T.W. and X.H. analyzed the data; L.S. wrote the manuscript draft; H.X., C.L., and M.E. reviewed and edited the manuscript. All authors have read and agreed to the published version of the manuscript.

295   *Competing interests.* The authors declare that they have no conflict of interest.

Copyright statements. The copyright statement will be included by Copernicus.

Acknowledgements. Thanks for the support of the Xinjiang Uygur Autonomous Region Meteorological Service and the Desert Meteorological Institute of China Meteorological Administration for this experiment and local meteorological data. The National Satellite Meteorological Center of the China Meteorological Administration for providing support with the cloud

300 product data. The European Centre for Medium-Range Weather Forecasts for providing support with atmospheric reanalysis data.

References

Abshire, N., Schwiesow, R., and Derr, V.: Doppler lidar observations of hydrometeors, Journal of Applied Meteorology, 13, 951-953, https://doi.org/10.1175/1520-0450(1974)013<0951:DLOOH>2.0.CO;2, 1974.

305 Alexander, S. and Protat, A.: Cloud properties observed from the surface and by satellite at the northern edge of the Southern Ocean, Journal of Geophysical Research: Atmospheres, 123, 443-456, https://doi.org/10.1002/2017JD026552, 2018.

Ansmann, A., Mattis, I., Müller, D., Wandinger, U., Radlach, M., Althausen, D., and Damoah, R.: Ice formation in Saharan dust over central Europe observed with temperature/humidity/aerosol Raman lidar, Journal of Geophysical Research: Atmospheres, 110, D18S12, https://doi.org/10.1029/2004JD005000, 2005.

310 Ansmann, A., Tesche, M., Seifert, P., Althausen, D., Engelmann, R., Fruntke, J., Wandinger, U., Mattis, I., and Müller, D.: Evolution of the ice phase in tropical altocumulus: SAMUM lidar observations over Cape Verde, Journal of Geophysical Research: Atmospheres, 114, https://doi.org/10.1029/2008JD011659, 2009.

Ansmann, A., Tesche, M., Althausen, D., Müller, D., Seifert, P., Freudenthaler, V., Heese, B., Wiegner, M., Pisani, G., and Knippertz, P.: Influence of Saharan dust on cloud glaciation in southern Morocco during the Saharan Mineral Dust Experiment, Journal of Geophysical

315 Research: Atmospheres, 113, D04210, https://doi.org/10.1029/2007JD008785, 2008.

Banakh, V., Smalikho, I., and Falits, A.: Estimation of the turbulence energy dissipation rate in the atmospheric boundary layer from measurements of the radial wind velocity by micropulse coherent Doppler lidar, Optics Express, 25, 22679-22692, https://doi.org/10.1364/OE.25.022679, 2017.

Bessho, K., Date, K., Hayashi, M., Ikeda, A., Imai, T., Inoue, H., Kumagai, Y., Miyakawa, T., Murata, H., and Ohno, T.: An introduction to

320 Himawari-8/9—Japan's new-generation geostationary meteorological satellites, Journal of the Meteorological Society of Japan. Ser. II, 94, 151-183, https://doi.org/10.2151/jmsj.2016-009, 2016.

Cheng, C. and Yi, F.: Falling mixed-phase ice virga and their liquid parent cloud layers as observed by ground-based lidars, Remote Sensing, 12, 2094, https://doi.org/10.3390/rs12132094, 2020.

Chouza, F., Reitebuch, O., Benedetti, A., and Weinzierl, B.: Saharan dust long-range transport across the Atlantic studied by an airborne

325 Doppler wind lidar and the MACC model, Atmos Chem Phys, 16, 11581-11600, https://doi.org/10.5194/acp-16-11581-2016, 2016.

DeMott, P. J., Finnegan, W. G., and Grant, L. O.: An Application of Chemical Kinetic Theory and Methodology to Characterize the Ice Nucleating Properties of Aerosols Used for Weather Modification, Journal of Applied Meteorology and Climatology, 22, 1190–1203, https://doi.org/10.1175/1520-0450(1983)022<1190:AAOCKT>2.0.CO;2, 1983.

Field, P. R.: Aircraft observations of ice crystal evolution in an altostratus cloud, Journal of the Atmospheric Sciences, 56, 1925-1941,

330 https://doi.org/10.1175/1520-0469(1999)056<1925:AOOICE>2.0.CO;2, 1999.

Gelaro, R., McCarty, W., Suárez, M. J., Todling, R., Molod, A., Takacs, L., Randles, C. A., Darmenov, A., Bosilovich, M. G., Reichle, R., Wargan, K., Coy, L., Cullather, R., Draper, C., Akella, S., Buchard, V., Conaty, A., da Silva, A. M., Gu, W., Kim, G.-K., Koster, R., Lucchesi, R., Merkova, D., Nielsen, J. E., Partyka, G., Pawson, S., Putman, W., Rienecker, M., Schubert, S. D., Sienkiewicz, M., and Zhao, B.: The Modern-Era Retrospective Analysis for Research and Applications, Version 2 (MERRA-2), Journal of Climate, 30, 5419-5454,

335 https://doi.org/10.1175/JCLI-D-16-0758.1, 2017.

Gultepe, I., Heymsfield, A., Field, P., and Axisa, D.: Ice phase precipitation, Meteorological Monographs, 58, 6.1-6.36, https://doi.org/10.1175/AMSMONOGRAPHS-D-16-0013.1, 2017.

Harvey, N. J., Hogan, R. J., and Dacre, H. F.: A method to diagnose boundary-layer type using Doppler lidar, Quarterly Journal of the Royal Meteorological Society, 139, 1681-1693, https://doi.org/10.1002/qj.2068, 2013.

340 He, Q., Li, J., Zhao, T., Zhang, H., and Meng, L.: Observing a dust aerosol layer at a height of 3–4 km above the ground on the southern margin of the Tarim Basin, Atmospheric Environment, 318, 120236, https://doi.org/10.1016/j.atmosenv.2023.120236, 2023.

He, Y., Liu, F., Yin, Z., Zhang, Y., Zhan, Y., and Yi, F.: Horizontally oriented ice crystals observed by the synergy of zenith-and slant-pointed polarization lidar over Wuhan (30.5° N, 114.4° E), China, Journal of Quantitative Spectroscopy and Radiative Transfer, 268, 107626, https://doi.org/10.1016/j.jqsrt.2021.107626, 2021.

345 Heese, B., Flentje, H., Althausen, D., Ansmann, A., and Frey, S.: Ceilometer lidar comparison: backscatter coefficient retrieval and signal-to-noise ratio determination, Atmospheric Measurement Techniques, 3, 1763-1770, https://doi.org/10.5194/amt-3-1763-2010, 2010.

Hersbach, H., Bell, B., Berrisford, P., Hirahara, S., Horányi, A., Muñoz-Sabater, J., Nicolas, J., Peubey, C., Radu, R., and Schepers, D.: The ERA5 global reanalysis, Quarterly Journal of the Royal Meteorological Society, 146, 1999-2049, https://doi.org/10.1002/qj.3803, 2020.

Heymsfield, A. J.: Production of ice in tropospheric clouds:A Review, Bulletin of the American Meteorological Society, 86, 795–808,

350 https://doi.org/10.1175/BAMS-86-6-795, 2005.

Holtslag, A. and Boville, B.: Local versus nonlocal boundary-layer diffusion in a global climate model, Journal of Climate, 6, 1825-1842, https://doi.org/10.1175/1520-0442(1993)006<1825:LVNBLD>2.0.CO;2, 1993.

Huang, J., Wang, T., Wang, W., Li, Z., and Yan, H.: Climate effects of dust aerosols over East Asian arid and semiarid regions, Journal of Geophysical Research: Atmospheres, 119, 11,398 - 311,416, https://doi.org/10.1002/2014JD021796, 2014.

355 Jiang, P., Yuan, J., Wu, K., Wang, L., and Xia, H.: Turbulence detection in the atmospheric boundary layer using coherent Doppler wind lidar and microwave radiometer, Remote Sensing, 14, 2951, https://doi.org/10.5194/amt-2021-288, 2022.

Kanji, Z. A., Ladino, L. A., Wex, H., Boose, Y., Burkert-Kohn, M., Cziczo, D. J., and Krämer, M.: Overview of Ice Nucleating Particles, Meteorological Monographs, 58, 1.1–1.33, https://doi.org/10.1175/AMSMONOGRAPHS-D-16-0006.1, 2017.

Klein, H., Nickovic, S., Haunold, W., Bundke, U., Nillius, B., Ebert, M., Weinbruch, S., Schuetz, L., Levin, Z., and Barrie, L.: Saharan dust
360 and ice nuclei over Central Europe, Atmos Chem Phys, 10, 10211-10221, https://doi.org/10.5194/acp-10-10211-2010, 2010.

Lai, R., Teng, S., Yi, B., Letu, H., Min, M., Tang, S., and Liu, C.: Comparison of Cloud Properties from Himawari-8 and FengYun-4A Geostationary Satellite Radiometers with MODIS Cloud Retrievals, Remote Sensing, 11, 1703, https://doi.org/10.3390/RS11141703, 2019.

Li, M., Xia, H., Su, L., Han, H., Wang, X., and Yuan, J.: The Detection of Desert Aerosol Incorporating Coherent Doppler Wind Lidar and
365 Rayleigh-Mie-Raman Lidar, Remote Sensing, 15, 5453, https://doi.org/10.3390/rs15235453, 2023.

Li, Z., Niu, F., Fan, J., Liu, Y., Rosenfeld, D., and Ding, Y.: Long-term impacts of aerosols on the vertical development of clouds and precipitation, Nature Geoscience, 4, 888-894, https://doi.org/10.1038/NGEO1313, 2011.

Liu, H., Yuan, L., Fan, C., Liu, F., Zhang, X., Zhu, X., Liu, J., Zhu, X., and Chen, W.: Performance validation on an all-fiber 1.54-μ m pulsed coherent Doppler lidar for wind-profile measurement, Optical Engineering, 59, 014109, https://doi.org/10.1117/1.OE.59.1.014109,
370 2020.

Liu, Z., Dong, Z., Zhang, Z., Cui, X., and Xiao, N.: Spatial and temporal variation of the near-surface wind regimes in the Taklimakan Desert, Northwest China, Theoretical and Applied Climatology, 138, 433-447, https://doi.org/10.1007/s00704-019-02824-w, 2019.

Lloyd, G., Choularton, T. W., Bower, K. N., Gallagher, M. W., Connolly, P. J., Flynn, M., Farrington, R., Crosier, J., Schlenczek, O., and Fugal, J.: The origins of ice crystals measured in mixed-phase clouds at the high-alpine site Jungfraujoch, Atmos Chem Phys, 15, 12953-
375 12969, https://doi.org/10.5194/acp-15-12953-2015, 2015.

Ma, Y., Gong, W., and Mao, F.: Transfer learning used to analyze the dynamic evolution of the dust aerosol, Journal of Quantitative Spectroscopy and Radiative Transfer, 153, 119-130, https://doi.org/10.1016/j.jqsrt.2014.09.025, 2015.

Manninen, A. J., Marke, T., Tuononen, M., and O'Connor, E. J.: Atmospheric Boundary Layer Classification With Doppler Lidar, Journal of Geophysical Research: Atmospheres, 123, 8172-8189, https://doi.org/10.1029/2017JD028169, 2018.

380 Moore, E. B. and Molinero, V.: Structural transformation in supercooled water controls the crystallization rate of ice, Nature, 479, 506-508, https://doi.org/10.1038/nature10586, 2011.

Morris, C. E., Georgakopoulos, D. G., and Sands, D. C.: Ice nucleation active bacteria and their potential role in precipitation, Journal De Physique Iv, 121, 87-103, https://doi.org/10.1051/jp4:2004121004, 2004.

Murray, B., O'sullivan, D., Atkinson, J., and Webb, M.: Ice nucleation by particles immersed in supercooled cloud droplets, Chemical
385 Society Reviews, 41, 6519-6554, https://doi.org/10.1039/c2cs35200a, 2012.

Pea, Gryning, S.-E., Hahmann, and A., N.: Observations of the atmospheric boundary layer height under marine upstream flow conditions at a coastal site, Journal of Geophysical Research: Atmospheres, 118, 1924-1940, https://doi.org/10.1002/jgrd.50175, 2013.

Ramanathan, V., Crutzen, P. J., Kiehl, J., and Rosenfeld, D.: Aerosols, climate, and the hydrological cycle, science, 294, 2119-2124, https://doi.org/10.1126/science.106403, 2001.

390 Rogers, D. C. and Vali, G.: Ice crystal production by mountain surfaces, Journal of Applied Meteorology and Climatology, 26, 1152-1168, https://doi.org/10.1175/1520-0450(1987)026<1152:ICPBMS>2.0.CO;2, 1987.

Rosenfeld, D., Rudich, Y., and Lahav, R.: Desert dust suppressing precipitation: A possible desertification feedback loop, Proceedings of the National Academy of Sciences of the United States of America, 98, 5975-5980, https://doi.org/10.1073/pnas.10112279, 2001.

Rosenfeld, D., Yu, X., Liu, G., Xu, X., Zhu, Y., Yue, Z., Dai, J., Dong, Z., Dong, Y., and Peng, Y.: Glaciation temperatures of convective
395 clouds ingesting desert dust, air pollution and smoke from forest fires, Geophysical Research Letters, 38, https://doi.org/10.1029/2011GL049423, 2011.

Seifert, P., Ansmann, A., Mattis, I., Wandinger, U., Tesche, M., Engelmann, R., Müller, D., Pérez, C., and Haustein, K.: Saharan dust and heterogeneous ice formation: Eleven years of cloud observations at a central European EARLINET site, Journal of Geophysical Research: Atmospheres, 115, D20201, https://doi.org/10.1029/2009JD013222, 2010.

400 Shuoqiu, W. and Xiaoyan, M.: Analysis of dust vertical and horizontal distribution during dust events in northwest China based on FY-4A, MODIS and CALIPSO satellite data, Acta Scientiae Circumstantiae, 40, 2892-2901, https://doi.org/10.13671/j.hjkxxb.2020.0093, 2020.

Stein, A. F., Draxler, R. R., Rolph, G. D., Stunder, B. J. B., Cohen, M. D., and Ngan, F.: NOAA's HYSPLIT Atmospheric Transport and Dispersion Modeling System, Bulletin of the American Meteorological Society, 96, 2059-2077, https://doi.org/10.1175/BAMS-D-14-00110.1, 2015.

30

405   Su, L., Lu, C., Yuan, J., Wang, X., He, Q., and Xia, H.: Measurement report: The promotion of the low-level jet and thermal effects on the development of the deep convective boundary layer at the southern edge of the Taklimakan Desert, Atmos. Chem. Phys., 24, 10947-10963, https://doi.org/10.5194/acp-24-10947-2024, 2024a.

Su, L., Xia, H., Yuan, J., Wang, Y., Maituerdi, A., and He, Q.: Study on Daytime Atmospheric Mixing Layer Height Based on 2-Year Coherent Doppler Wind Lidar Observations at the Southern Edge of the Taklimakan Desert, Remote Sensing, 16, 3005,
410   https://doi.org/10.3390/rs16163005, 2024b.

Su, L., Xia, H., Lu, C., Yuan, J., Wu, K., Wei, T., Wang, X., Elshora, M., and He, Q.: Study on the life cycle of ice crystal cloud over the Taklimakan desert using multi-source data, Figshare [dataset], 10.6084/m9.figshare.25432984.v1, 2024c.

Sullivan, S., Voigt, A., Miltenberger, A., Rolf, C., and Krämer, M.: A Lagrangian perspective of microphysical impact on ice cloud evolution and radiative heating, Journal of Advances in Modeling Earth Systems, 14, e2022MS003226, https://doi.org/10.1029/2022MS003226,
415   2022.

Sun, J. and Liu, T.-s.: The Age of the Taklimakan Desert, Science, 312, 1621-1621, https://doi.org/10.1126/science.112461, 2006.

Tang, D., Wei, T., Yuan, J., Xia, H., and Dou, X.: Observation of bioaerosol transport using wideband integrated bioaerosol sensor and coherent Doppler lidar, Atmospheric Measurement Techniques, 15, 2819-2838, 2022.

Tao, W. K., Chen, J. P., Li, Z., Wang, C., and Zhang, C.: Impact of aerosols on convective clouds and precipitation, Reviews of Geophysics,
420   50, RG2001, https://doi.org/10.1029/2011RG000369, 2012.

Vali, G.: Nucleation terminology, Bulletin of the American Meteorological Society, 66, 1426-1427, 1985.

Wang, L., Yuan, J., Xia, H., Zhao, L., and Wu, Y.: Marine mixed layer height detection using ship-borne coherent Doppler wind lidar based on constant turbulence threshold, Remote Sensing, 14, 745, https://doi.org/10.3390/rs14030745, 2022.

Wang, L., Qiang, W., Xia, H., Wei, T., Yuan, J., and Jiang, P.: Robust Solution for Boundary Layer Height Detections with Coherent
425   Doppler Wind Lidar, Advances in Atmospheric Sciences, 38, 1920-1928, https://doi.org/10.1007/s00376-021-1068-0, 2021.

Wei, T., Xia, H., Hu, J., Wang, C., Shangguan, M., Wang, L., Jia, M., and Dou, X.: Simultaneous wind and rainfall detection by power spectrum analysis using a VAD scanning coherent Doppler lidar, Optics express, 27, 31235-31245, https://doi.org/10.1364/OE.27.031235, 2019.

Westbrook, C. and Illingworth, A.: The formation of ice in a long-lived supercooled layer cloud, Quarterly Journal of the Royal
430   Meteorological Society, 139, 2209-2221, https://doi.org/10.1002/qj.2096, 2013.

Westbrook, C., Illingworth, A., O'Connor, E., and Hogan, R.: Doppler lidar measurements of oriented planar ice crystals falling from supercooled and glaciated layer clouds, Quarterly Journal of the Royal Meteorological Society, 136, 260-276, https://doi.org/10.1002/qj.528, 2010.

Wu, C. and Yi, F.: Local ice formation via liquid water growth in slowly ascending humid aerosol/liquid water layers observed with
435   ground- based lidars and radiosondes, Journal of Geophysical Research: Atmospheres, 122, 4479-4493, https://doi.org/10.1002/2016JD025765, 2017.

Wu, K., Wei, T., Yuan, J., Xia, H., Huang, X., Lu, G., Zhang, Y., Liu, F., Zhu, B., and Ding, W.: Thundercloud structures detected and analyzed based on coherent Doppler wind lidar, Atmospheric Measurement Techniques, 16, 5811-5825, https://doi.org/10.5194/amt-16-5811-2023, 2023.

440   Wu, S., Song, X., Liu, B., Dai, G., Liu, J., Zhang, K., Qin, S., Hua, D., Gao, F., and Liu, L.: Mobile multi-wavelength polarization Raman lidar for water vapor, cloud and aerosol measurement, Optics express, 23, 33870-33892, https://doi.org/10.1364/OE.23.033870, 2015.

Yang, J., Zhang, Z., Wei, C., Lu, F., and Guo, Q.: Introducing the New Generation of Chinese Geostationary Weather Satellites, Fengyun-4, Bulletin of the American Meteorological Society, 98, 1637-1658, https://doi.org/10.1175/BAMS-D-16-0065.1, 2017.

Yang, X., Shen, S., Yang, F., He, Q., Ali, M., Huo, W., and Liu, X.: Spatial and temporal variations of blowing dust events in the Taklimakan
445   Desert, Theoretical and Applied Climatology, 125, 669-677, https://doi.org/10.1007/s00704-015-1537-4, 2016.

Yin, Z., Yi, F., He, Y., Liu, F., Yu, C., Zhang, Y., and Wang, W.: Asian dust impacts on heterogeneous ice formation at Wuhan based on polarization lidar measurements, Atmospheric Environment, 246, 118166, https://doi.org/10.1016/j.atmosenv.2020.118166 2021.

Yoshida, R., Okamoto, H., Hagihara, Y., and Ishimoto, H.: Global analysis of cloud phase and ice crystal orientation from Cloud-Aerosol Lidar and Infrared Pathfinder Satellite Observation (CALIPSO) data using attenuated backscattering and depolarization ratio, Journal of
450   Geophysical Research, 115, D00H32, https://doi.org/10.1029/2009JD012334, 2010.

Yuan, J., Xia, H., Wei, T., Wang, L., Yue, B., and Wu, Y.: Identifying cloud, precipitation, windshear, and turbulence by deep analysis of the power spectrum of coherent Doppler wind lidar, Optics Express, 28, 37406-37418, https://doi.org/10.1364/OE.412809, 2020.

Yuan, J., Su, L., Xia, H., Li, Y., Zhang, M., Zhen, G., and Li, J.: Microburst, windshear, gust front, and vortex detection in mega airport using a single coherent Doppler wind lidar, Remote Sensing, 14, 1626, https://doi.org/10.3390/rs14071626, 2022a.

455   Yuan, Y., Di, H., Liu, Y., Yang, T., Li, Q., Yan, Q., Xin, W., Li, S., and Hua, D.: Detection and analysis of cloud boundary in Xi'an, China, employing 35 GHz cloud radar aided by 1064 nm lidar, Atmospheric Measurement Techniques, 15, 4989-5006, https://doi.org/10.5194/amt-15-4989-2022, 2022b.

Zeng, X., Tao, W., Zhang, M., Hou, A., Xie, S., Lang, S. E., Li, X., Starr, D., and Li, X.: A contribution by ice nuclei to global warming, Quarterly Journal of the Royal Meteorological Society, 135, https://doi.org/10.1002/qj.449, 2009.

460   Zhang, Y., Wu, Y., and Xia, H.: Spatial resolution enhancement of coherent Doppler wind lidar using differential correlation pair technique, Optics Letters, 46, 5550-5553, https://doi.org/10.1109/jlt.2022.3160294, 2021.